Analysis of a Dynamic Model for Post-Combustion CO2 Capture on a Hollow Fiber Membrane Contactor

Wanderson Passos *, Arioston Júnior , José Filho , Leopoldo Rojas

Posted Date: 29 December 2023

doi: 10.20944/preprints202312.2309.v1

Keywords: HFMC; carbon capture; modelling, and simulation; system dynamics; post-combustion

Article

Analysis of a Dynamic Model for Post-Combustion CO_2 Capture on a Hollow Fiber Membrane Contactor

Wanderson Passos [1,*], Arioston Júnior [1], José Filho [2] and Leopoldo Rojas [1]

[1] Graduate Program in Chemical Engineering, Federal University of Paraíba, João Pessoa, Brazil; aamj@ct.ufpb@ufpb.br (A.J.); leopoldo@ct.ufpb.br (L.R.)

[2] Chemical Engineering Department, Federal University of Paraíba, João Pessoa, Brazil; carlosdeniz14@gmail.com

* Correspondence: wanderson_f000@outlook.com; Tel.: +55-81-99570-0501

Abstract: The Hollow fiber membrane contactor (HFMC) is an intensification process that combines membrane and absorption technologies, being a technology in expansion, so the dynamics of this process is crucial for an increase in industrial scale-up. In this manuscript a rigorous dynamic model of an HFMC is developed and simulated in Python software for the absorption of post-combustion CO_2 using a monoethanolamine (MEA) solution, which was validated using available data in literature in steady state. Dynamic simulations were performed to analyze the model's capability to predict the effect of disturbances on the responses of CO_2 capture ratio and loading. Four distinct experiments were conducted by step changes and pulse disturbances at the following variables: gas and liquid volumetric flow rates, CO_2 composition in flue gases, and CO_2 lean load. The gas phase showed a faster response compared to the liquid. The CO_2 capture ratio and rich loading presented opposite responses when disturbing both liquid flows, and for the composition and lean loading variations, the capture ratio presented an inverse response characteristic, while the loading showed a delayed response. As the model proved to be capable of returning to the reference state, it can potentially be used for control studies purposes.

Keywords: HFMC; carbon capture; modelling; and simulation; system dynamics; post-combustion

1. Introduction

The Greenhouse Effect has been growing along the last decades, due to the ascending of power generation by combustion of fossil fuels, such as coal, natural gas an oil. Between the greenhouse gases, the one who has the most contribution is carbon dioxide (CO_2), which contributes around 55 percent for the effects of the global warming [1,2]. Consequently, a large amount of research has been developed to study new technologies for carbon capture and storage (CCS), in order to mitigate the amount of CO_2 emissions into the atmosphere. Post-combustion carbon capture processes are mature, effective, and currently the basis for CCS developments [3], as they offer some advantages if compared to others, such as retrofitting facility [4]. From these processes, the CO_2 chemical absorption in alkanolamines leads the market of carbon capture [5–7].

The mentioned process uses conventional equipment such as absorption columns, which although have been leading the research for carbon capture, still present some disadvantages, such as the large amount of energy consumption, liquid losses, and foaming [5,8–11]. To overcome these disadvantages some modifications are proposed. A potential alternative the membrane separation process, in what [4] has separated in two different categories: membrane-based separation and membrane gas absorption (MGA). The first one is related to the separation processes where the membranes provide the selectivity themselves, and the mass transport is given purely by Knudsen diffusion and driven by the partial pressure gradient [12]; whereas in the last one, the membranes may provide or not an additional selectivity, acting as gas-liquid contacting devices. MGA is also known as membrane contactor technology, which is widely carried out in units called Hollow Fiber Membrane Contactors (HFMC) for CO_2 absorption [7]. Many advantages of this equipment are listed in relation to conventional technologies used for liquid-gas and liquid-liquid separations, such as

 doi:10.20944/preprints202312.2309.v1

constant interfacial area, no emulsion formation, facility in scaling-up and substantially higher efficiency [13]. Also, the smaller energy consumption can be added to the list [14,15].

HFMCs can be modeled and designed through many ways, being operated in a counter-current, cross or co-current flows, and using one, two or three-dimensional modeling approaches [16,17], and several, experimental and theoretical works, have been published. In the experimental field the chemical absorption of CO_2 in HFMCs using different types of absorbents, such as water, monoethanolamine, diethanolamine and trifluoro-acetylacetone were investigated [7,18]. On theoretical issues, [19] proposed a generic one-dimensional model under isothermal conditions, which was compared to bidimensional approach by [20]. An HFMC model in adiabatic and one-dimensional condition was evaluated by [21,22].

With respect to the transient approach, [23] analyzed the transient results of a membrane contactor operating in parallel flux against some disturbances in properties that cannot be controlled in transient conditions. [24] studies a model for membrane contactors concentrated only on time and compares the unit approach with a cell-based approach. Another cell approach is proposed by [25], where the absorption of CO_2 is compared using different solvents: water, 2-amino-2-methyl-1-propanol (AMP) and dimethylamine (DEA). A recent work developed by [26] analyzes the dynamic performance of a membrane module for CO_2 separation using a gas-gas system, by step changes in the operating conditions. In another recent work, a non-isothermal dynamic model for capture CO_2 from natural gas is presented by [27], despite carrying out robust modeling, the work lacks analysis of responses to important disturbances in the process.

With the growing development of membrane systems in either laboratory or pilot scales, and further industrial applications, it is necessary to study the dynamic behavior of this units to start applying subsequent control strategies to these processes. Previous research focused on simple rate-based or Computational fluid dynamics (CFD) modeling (which requires a great computational effort), even when one-dimensional approaches can give satisfactory results, and using relatively robust solutions for accurate design results, but cannot be used to easy apply control algorithms. Therefore, this paper aims to propose a dynamic, one-dimensional, and isothermal model of a hollow fiber membrane contactor unit for post-combustion CO_2 capture and analyze the dynamic behavior of the model and its capability to coherently predict the effects against some disturbances applied to several input variables. Also, this manuscript discusses about the possible explanations that may lead to many different dynamic profiles in the system at various conditions and inputs changes.

2. System features

The system consists in a hollow fiber membrane contactor (HFMC), which can be de-scribed as a bundle of long and narrow hollow tubular fibers inside a shell [17], such as a conventional shell and tube heat exchanger, as illustrated on Figure 1. The gaseous stream (flue gas flow rate), which is entering on the shell side of the HFMC, is a mixture of carbon dioxide (CO_2), nitrogen (N_2), oxygen (O_2) and water vapor (H_2O), as it commonly describes a post-combustion stream composition [7,28–30]. The liquid stream is leaking on the lumen side and consists in an aqueous solution of monoethanolamine (MEA) 30% (w/w). This solvent has high a CO_2 uptake due to its affinity and the chemical conversion with MEA in the liquid phase [4,17].

Preprints (www.preprints.org) | NOT PEER-REVIEWED | Posted: 29 December 2023 doi:10.20944/preprints202312.2309.v1

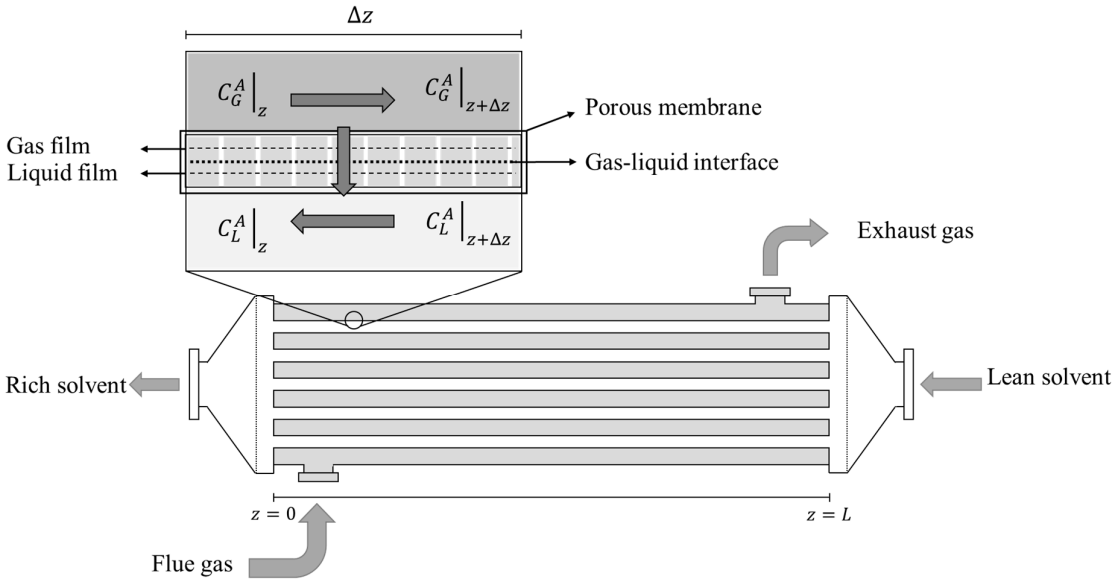

Figure 1. Schematic representation of a Hollow fiber membrane contactor illustration.

2.1. Geometry and flow

Capillary fibers present high area-volume ratios exhibiting large areas that improves the mass transfer processes. The pilot plant and the laboratory unit studied by [31,32] were used for the simulation - dynamic analysis and the validation purpose. Thus, the fiber volume fraction (or packing fraction) of the HFMC was fixed (around φ=0.6), as it is typically used in conventional contactors for lab or pilot scale [4,7,19,20,22,32–34]. Both the internal and external membrane radii (r_i and r_e, respectively) were fixed. The radii difference defines the membrane thickness (δ) and the relative membrane thickness as the ratio between the membrane thickness to the external radio (δ/r_e). With the previous parameters defined, the shell radius (r_s) was calculated using Happel's free surface model [7,20,35].

Hydraulic diameters were used to describe the flow in the lumen and in the shell side, since the sections are circular. The total flow section areas for the gas and liquid phases were calculated using the module packing fraction, the membrane radius, and the number of fibers. Given the gas and liquid volumetric flow rates and the respective flow areas, the inlet velocities could be calculated. Table 1 shows the expressions used to estimate the parameters used.

Table 1. Expressions for geometrical characteristics of the system.

Parameter	Expression	Units	References
Shell radius	$r_s = r_e\sqrt{\frac{N_t}{\varphi}}$	n	[36]
Gas flow sectional area	$A_G^t = \pi r_s^2(1-\varphi)$	m²	-
Total liquid flow sectional area	$A_L^t = N_t \pi r_i^2$	m²	-
External hydraulic diameter	$d_{ext}^h = 2r_e\left(\frac{1-\varphi}{\varphi}\right)$	m	[20]
Internal hydraulic diameter	$d_{int}^h = 2r_e\left(1-\frac{\delta}{r_e}\right)$	m	[20]

Preprints (www.preprints.org) | NOT PEER-REVIEWED | Posted: 29 December 2023 doi:10.20944/preprints202312.2309.v1

2.2. Main model hypothesis

Important model assumptions (flow, system, membrane characteristics, thermodynamics, mass transfer and kinetics) are summarized in Table 2.

Table 2. General model assumptions.

Condition	Description
Flow	1. The configuration is in a counter-current flow. 2. Gas flows in the shell and liquid in the lumen.
System constraints	3. The regime is in unsteady state 4. Pressure drop is neglected for both phases. 5. Isothermal conditions are prevailed 6. The solvent evaporation and gas condensation were neglected
Membranes	7. Hydrophobic membrane pores with partial wetting operation.
Thermodynamics	8. Henry's Law is applicable at the interface gas-liquid (located at internal surface). 9. N_2 solubility neglected
Mass transfer	10. Uniform wall flux along the fibers
Chemical reaction	11. Irreversible, bimolecular, and second-order kinetics.

With the conditions and descriptions in Table 1, the system operates in a counter-current flow, with constant temperature and negligible pressure drop [19,20,23,24,36–38]. CO_2 concentration changes in gas and liquid currents does not affect their properties, keeping the flow rate constant along the process. It was assumed that the membrane tubes are microporous, given the need to allow greater selectivity in relation to CO_2 [4]. [39,40] analyzed the effect of pore wetting, and they concluded that, depending on the liquid pressure, this phase liquid could enter the pores, increasing the resistance to mass transfer, even in a very small percentage of wetting. In this paper, the membrane wetting was set in 5%, which showed to fit in this system. Considering the high affinity of the solvent with CO_2, the solubility of N_2 was neglected [33].

3. Model development

This section will present the main equations used to construct the dynamic model of the hollow fiber membrane contactor, which include concentrations, mass transfer, and chemical reaction conditions.

3.1. Component mas balance equations

For the mixture, the molar continuity equation for a species *i* is given by Eq. (1).

$$\frac{\partial C_i}{\partial t} = -\nabla \cdot \bar{N}_i + R_i''' \quad (1)$$

where C_i is the molar concentration of i (mol.m^{-3}), $\bar{N}_i$ is the molar flux vector of i (mol.m^{-2}s^{-1}) and R_i''' is the reaction rate for i (mol.m^{-3}s^{-1}). Considering only the axial velocity (cylindrical coordinates), describing the molar flux by the overall mass transfer coefficient, and neglecting the reaction rate, the molar balance for CO_2 on the gas phase is given by Eq. (2).

$$\frac{\partial C_G^A}{\partial t} = -v_G \frac{\partial C_G^A}{\partial z} - a_i E K_{OV} (C_G^A - C_L^A/m) \quad (2)$$

where C is the molar concentration of the component (mol/m^3), the superscript A represents de solute (CO_2), K_{OV} stands for the overall mass transfer coefficient (m.s^{-1}), the term a_i is the specific interfacial area (m^2/m^3), E is the enhancement factor, m is the volumetric partition coefficient, v is

Preprints (www.preprints.org) | NOT PEER-REVIEWED | Posted: 29 December 2023 doi:10.20944/preprints202312.2309.v1

the velocity of the fluid (m/s), and the subscripts G and L indicates the gas and liquid phases, respectively.

Henry's law was applied to describe the equilibrium at the gas-liquid interface, and the concentration of CO_2 at the internal surface of the fibers is a function of the liquid-gas volumetric partition coefficient (m), which is defined by the inverse of the dimensionless Henry constant for CO_2 on MEA solution as follows.

$$m = \frac{RT}{H_A} \tag{3}$$

For the liquid phase, the molar balance is like the previous one, however, the reaction term is not neglected, and the CO_2 molar flux is positive. Thus, considering a counter-current flow, the equation can be expressed by:

$$\frac{\partial C_L^A}{\partial t} = v_L \frac{\partial C_L^A}{\partial z} + a_i E K_{OV} (C_G^A - C_L^A/m) + R_A''' \tag{4}$$

where R_A''' represents the consumption rate of CO2 by chemical reaction on the liquid phase.

The consumes of CO_2 by the chemical reaction depends also on the concentration of MEA on de liquid. So, an equation to define the concentration of the second reactant is required, and it can be expressed as follows:

$$\frac{\partial C_L^B}{\partial t} = v_L \frac{\partial C_L^B}{\partial z} + R_B''' \tag{5}$$

where B denotes the free MEA on the aqueous solution.

3.2. Component mas balance equations

The two-film theory in equilibrium with the gas-liquid interface is assumed, as shown in Figure 2. The mass transfer is described by the concept of resistances in series, and the overall mass transfer coefficient is given as [17,27,41]:

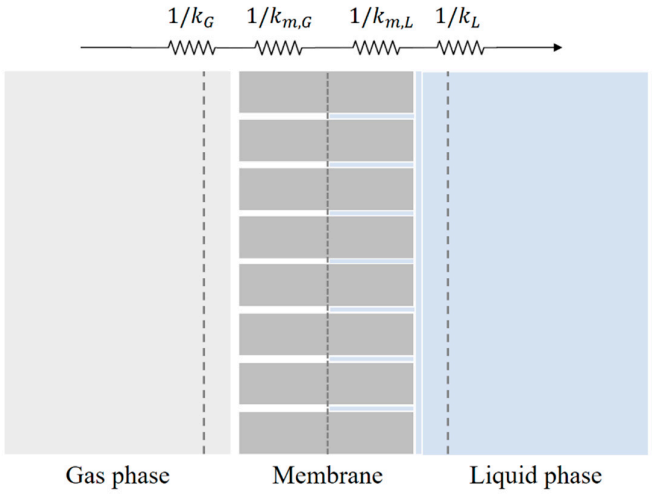

Figure 2. Gas, liquid, and membrane resistances in mass transfer.

$$\frac{1}{K_{OV}} = \frac{1}{k_G} + \frac{1 - e_p}{k_{m,G}} + \frac{e_p}{m k_{m,L}} + \frac{1}{m k_L} \tag{6}$$

where e_p is the wetting ratio (the fraction of wetted volume in the pores) and k stands for the mass transfer coefficient at each phase.

Therefore, the mass transfer coefficients for the phases were calculated using the Sherwood number given from different approaches of Graetz equation [13,33,42–45]. This approach was also

Preprints (www.preprints.org) | NOT PEER-REVIEWED | Posted: 29 December 2023 doi:10.20944/preprints202312.2309.v1

applied by [19,20,33,34] to estimate the local Sherwood number through the pack of cylinders, and consequently, the local mass transfer coefficient for the gas, and concludes that it is also suitable, considering laminar flow, fully developed profiles for and a uniform flux through the membrane.

The Sherwood (Sh) and Graetz (Gz) number for a species i in gas and liquid phases are correlated by Eqs. (7, 8), respectively, and defined by Eqs. (9, 10) for a fluid F.

$$Sh_G = \left(4.36^3 + 1.3^3 (Gz_G^{-1})\right)^{1/3} \tag{7}$$

$$Sh_L = 1.62 Gz_L^{-1/3} \tag{8}$$

$$Gz_F = \frac{D_{i,F} z}{v_F d_h^2} \tag{9}$$

$$Sh_F = \frac{k_F d_h}{D_{j,F}} \tag{10}$$

The Eq. (11) is used to calculate the membrane mass transfer coefficient for a component i in fluid F (gas or liquid). In the membrane, the coefficients were estimated using the concept proposed by [46] and the approach for partial wetted mode, using the wetting ratio in the overall resistance (Eq. 6) by [41].

$$k_{m,F} = \frac{D_{i,F}}{\delta}\left(\frac{\varepsilon}{\tau}\right) \tag{11}$$

where $D_{i,F}$, is the diffusivity coefficient of i in a fluid, δ is the membrane thickness, ε is the membrane porosity and τ is the membrane tortuosity.

To monitor the CO_2 absorbed, the percentual capture ratio (Θ) was defined as the ratio of the solute uptake in the absorber to the solute input. In terms of the inlet and outlet gas mol fractions of the solute according to Eq. (12).

$$\Theta = \frac{y_A^{in} - y_A^{out}}{y_A^{in}} 100\% \tag{12}$$

The amount of CO_2 in the liquid phase is often described by the loading in solvent, which can be estimated, using the reaction stoichiometric [19] by Eq. (13)

$$\alpha = 0.5 - \frac{C_L^B M_{MEA}}{2 w_{MEA} \rho_L} \tag{13}$$

3.3. Kinetics

Since the kinetics between CO_2 and alkanolamines are often kinetically controlled, the overall reaction kinetics are considered being irreversible and having second order characteristics [47,48]. Thus, occurring in the liquid phase, the expression and kinetics are given by Eqs. (14, 15).

$$A + 2B \rightarrow B_2A \tag{14}$$

$$R_A''' = -k_r C_L^A C_L^B \tag{15}$$

where k_r is the kinetic constant ($m^3 s^{-1} mol^{-1}$).

According to the stoichiometric, the rate of the consumption of free MEA is:

$$R_B''' = 2R_A''' = -2k_r C_L^A C_L^B \tag{16}$$

The Hatta number (Ha) and the asymptotic enhancement factor were used to define the chemical reaction regime in the system and are calculated by Eq. (17) and (18), respectively [49,50].

$$Ha = \frac{\sqrt{D_{A,L} k_r C_L^B}}{k_L} \tag{17}$$

Preprints (www.preprints.org) | NOT PEER-REVIEWED | Posted: 29 December 2023 doi:10.20944/preprints202312.2309.v1

$$E_\infty = \left(1 + \frac{C_L^B D_{B,L}}{2mC_M^A D_{A,L}}\right) \quad (18)$$

where $\boldsymbol{D_{A,L}}$ and $\boldsymbol{D_{B,L}}$ are the diffusion coefficient for the CO_2 and MEA, respectively, in the aqueous solution. The regime types and their relationship to the mentioned dimensionless numbers are shown on Table 3.

Table 3. Definition of reaction regime.

Reaction regime	Relationship
Pseudo first-order reaction by the gas-liquid interface (reaction is limiting the process)	$E_\infty > 5Ha$
Fast second order reaction (mass transfer is partially limiting the process)	$5E_\infty > Ha > \frac{E_\infty}{5}$
Instantaneous reaction at the film (mass transfer is limiting the process)	$5E_\infty > Ha > \frac{E_\infty}{5}$

Therefore, the enhancement factor E can be calculated, following the [51] correlation, by Eqs. (19,20).

$$\alpha_1 = \sqrt{\left(\frac{D_{A,L}}{D_{B,L}}\right)} + \sqrt{\left(\frac{D_{A,L}}{D_{B,L}}\right)\left(\frac{C_L^B}{2mC_G^A}\right)} \quad (19)$$

$$E = 1 + (\alpha_1 - 1)\left[1 - \exp\left(-\frac{Ha - 1}{\alpha_1 - 1}\right)\right] \quad (20)$$

4. Numerical solution and validation parameters

The method of lines (MOL) was applied to solve the distributed-parameter model, which is represented by the partial differential equations (PDEs) Eqs. (2), (4), and (5). The PDEs were approximated to a set of ordinary differential equations (ODEs), where the spatial terms were discretized using backward finite differences for the gas and forward differences for the liquid phase. The ODEs system was implemented in the Python software and solved by the internal function *odeint*, a tool from *scipy.integrate* package. Figure 3 shows the computational flow chart used to solve the set of equations., and the boundary and initial conditions are defined on Table 4.

Preprints (www.preprints.org) | NOT PEER-REVIEWED | Posted: 29 December 2023 doi:10.20944/preprints202312.2309.v1

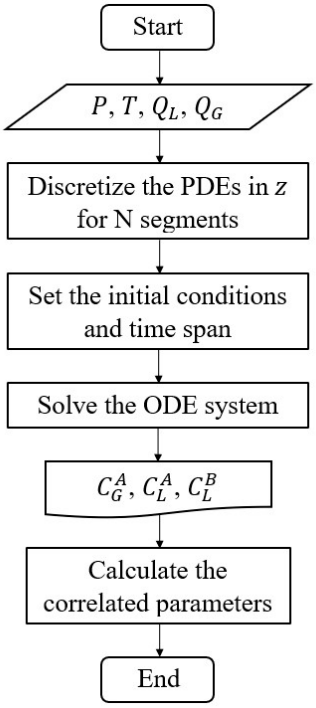

Figure 3. Computational flowchart.

Table 4. Boundary and initial conditions.

Parameter	Expression	Units
$t = 0$	$C_G^A = C_{G,0}^A$ $C_L^A = C_{L,0}^A$ $C_L^B = C_{L,0}^B$	for $0 \leq z \leq L$
$z = 0$	$C_G^A = C_{G,0}^A$	for $0 < t < \infty$
$z = L$	$C_L^A = C_{L,0}^A$ $C_L^B = C_{L,0}^B$	

The concentrations of the gaseous and liquid phases at the HFMC inlet or in the initial condition are indicated in Table 4 by the subscript 0 (zero).

Several works in the literature, using different approaches, solvents and configurations were already validated with experimental data [22,33,39,51,52]. These studies do not deal model validation with process dynamics data, due to the lack of pilot-scale or even laboratory-scale dynamic data in the literature.

Although this manuscript also does not validate the dynamic behavior, a steady-state validation was performed using the laboratory-scale data from [32], for a post-combustion CO_2 capture system by MEA solution. Also, pilot-plant specifications from a unit studied by [31,32] were used to perform the simulations and analyze the transient behavior. Both lab and pilot-scale specifications are summarized in Table 5.

Table 5. Units' specification.

	Parameter	Lab-scale	Pilot-scale
Module	Inner radius (m)	$r_s = 6{,}2 \times 10^{-3}$	$r_s = 5{,}25 \times 10^{-2}$
	Effective length (m)	$L = 0{,}30$	$L = 0{,}88$
	Number of fibers (-)	$N_t = 119$	$N_t = 8521$
	Packing ration (-)	$\varphi = 0{,}59$	$\varphi = 0{,}648$
	Specific interfacial area (m^2/m^3)	1331	1329
Fiber	Inner radius (m)	$r_i = 2{,}15 \times 10^{-4}$	

Preprints (www.preprints.org) | NOT PEER-REVIEWED | Posted: 29 December 2023 doi:10.20944/preprints202312.2309.v1

Outer radius (m)	$r_e = 4{,}35 \times 10^{-4}$
Porosity (-)	$\varepsilon = 0{,}336$
Material (-)	$PTFE$

The parameters correlations used in the simulations are summarized on Table 6.

Table 6. Parameter correlations and relations.

Parameter	Expression	Units	References
Henry constant for CO_2 in MEA solution	$H_A = H_{N_2O,MEA}\left(\frac{H_{A,water}}{H_{N_2O,water}}\right)$ $H_{i,j} = \exp\left(C_1 + \frac{C_2}{T} + C_3 \ln T + C_4 T\right)$ i: CO_2, N_2 j: water, MEA 30% (mass)	$Pa.m^3mol^{-1}$	[53]
Diffusion coefficient of CO_2 on gas mixture	$D_{A,G} = \left(\sum_i \frac{y_i}{D_{A,i}}\right)^{-1}$; $D_{A,i} = \frac{0.00143T^{1.75}}{PM_{A,i}^{1/2}\left[(\sum v)_A{}^{1/3} + (\sum v)_i{}^{1/3}\right]^2}$; $M_{A,i} = 2\left(\frac{1}{M_A} + \frac{1}{M_i}\right)^{-1}$ i: N_2, O_2, H_2O	m^2s^{-1}	[54]
Density of MEA solution	$\rho_L = \frac{\sum_i x_i M_i}{\sum_i (x_i \hat{V}_i) + x_{i=1}x_{i=2}\hat{V}^* + x_{i=1}x_{i=3}\hat{V}^{**}}$ i: MEA, H_2O, CO_2	$10^{-3}\,kg.m^{-3}$	[55]
Initial concentration of MEA	$C_{L,0}^B = \frac{w_{MEA}\rho_L}{M_{MEA}}$	$mol.m^{-3}$	-
Viscosity of MEA solution	$\mu_L = \exp\left[0.16C_{L,0}^B + 19.1\exp\left(-\frac{298.3}{T}\right)\right]$	Pa.s	[56]
Diffusion coefficient of CO_2 in MEA solution	$D_{A,L} = D_{A,water}\left(\frac{\mu_{water}}{\mu_L}\right)^{0.8}$	m^2s^{-1}	[57]
Diffusion coefficient of MEA in MEA solution	$D_{B,L} = \exp\left(-13.275 - \frac{2198.3}{T} - 7.8142 \times 10^{-5} C_{L,0}^B\right)$	m^2s^{-1}	[58]
Kinetic constant	$k_r = 4.4 \times 10^8 \exp\left(-\frac{5400}{T}\right)$	$m^3mol^{-1}s^{-1}$	[59]

5. Simulation results

The steady-state model is obtained by equating the terms on the left side of the equality in Eqs. (2), (4) and (5) to zero, this model was validated using laboratory scale data provided by [32] and the specifications in Table (5). The comparison was evaluated using the outlet CO_2 fraction (% CO_2) in the gas at different gas flow rates (Q_G) for two different liquid flow rates (Q_L). Figure 4 compares the

Preprints (www.preprints.org) | NOT PEER-REVIEWED | Posted: 29 December 2023 doi:10.20944/preprints202312.2309.v1

values for both cases. The profiles in Figure 4 shows a good agreement between the simulation results and the experimental data used, presenting a correlation coefficient $R^2 > 0,95$ for both cases. The simulation behavior of CO_2% as the Q_G changes follows the experimental pattern, as expected, for both QL values. The model proved to predict the absorption of post-combustion CO_2 in MEA solution using a HFMC, therefore validated for being used for intended analyses in this work.

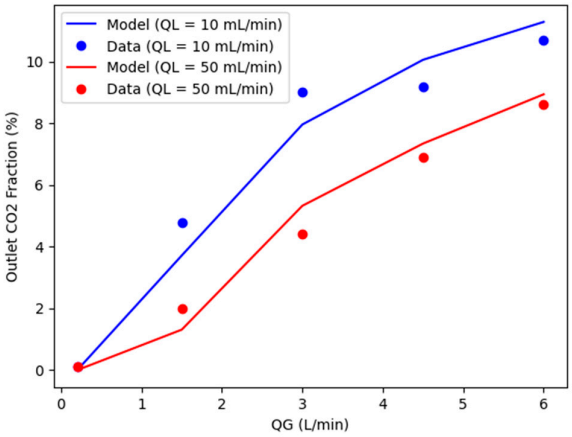

Figure 4. Comparison of simulated and experimental results in lab scale for gas flow range from 0.2 to 6.0 L/min and liquid flow rates of 10 (in blue) and 50 mL/min (in red).

5.1. System behavior

Following, the dynamics of the carbon capture plant is studied. The model is submitted to disturbances in the load and the changes in the operating conditions coming from the up-stream power plant. The initial conditions are given in Table 7, and the steady state reached in these conditions was further used as the base case to analyze the plant dynamics.

Table 7. Simulation parameters.

Parameter	Value or expression	Units
Operation pressure	$P = 1.05 \times 10^5$	Pa
Operation temperature	$T = 300.15$	K
Inlet volumetric rate of gas	$Q_G^{in} = 2{,}78 \times 10^{-3}$	m^3s^{-1}
Overall volumetric rate of liquid	$Q_L = 5{,}56 \times 10^{-5}$	m^3s^{-1}
Inlet molar fraction of CO_2 on gas	$y_A^{in} = 0.15$	-
Inlet molar fraction of N_2 on gas	$y_{N_2}^{in} = 1 - y_A^{in}$	
Inlet concentration of CO_2 on gas	$C_{G,0}^A = y_A^0 \frac{P}{RT}$	$mol.m^{-3}$
Inlet concentration of free CO_2 on liquid	$C_{L,0}^A = 0$	$mol.m^{-3}$
Mass fraction of MEA	$w_{MEA} = 0.3$	-
Inlet concentration of free MEA on liquid	$C_{L,0}^B = \frac{w_{MEA}\rho_L}{M_{MEA}}$	$mol.m^{-3}$
Lean loading of CO_2	$\alpha_0 = 0{,}218$	$mol_{CO2}.mol_{MEA}^{-1}$
Number of segments on discretized space	$N = 100$	-
Membrane tortuosity	$\tau = 1.0$	-
Wetting fraction	$e_p = 0.05$	-

The transient behavior of the membrane contactor for the given initial conditions (Table 4) is shown on Figure 5, as the solution of the equations, where five points from the discretized space were selected for visualization. It can be seen that the system reaches steady-state around 30 seconds. Furthermore, Figure 5(a) and (b) show the behavior of the so-lute in the gas and liquid phases, respectively, where they present a similar mirror trend: they both initially suffer an abrupt change,

Preprints (www.preprints.org) | NOT PEER-REVIEWED | Posted: 29 December 2023 doi:10.20944/preprints202312.2309.v1

which represents a peak in CO_2 molar flux, followed by a smooth increase, until reach the steady-state. As the amount of CO_2 in gas phase migrates instantaneously to de liquid phase, the chemical reaction starts do consume both free CO_2 and free MEA in liquid, and this decrease in free MEA concentration, showed in Figure 5 (c) provides a decrease also in the overall CO_2 molar flux. This reduction explains the smooth growth in the CO_2 concentration profiles and makes clear that the chemical reaction is also controlling the process.

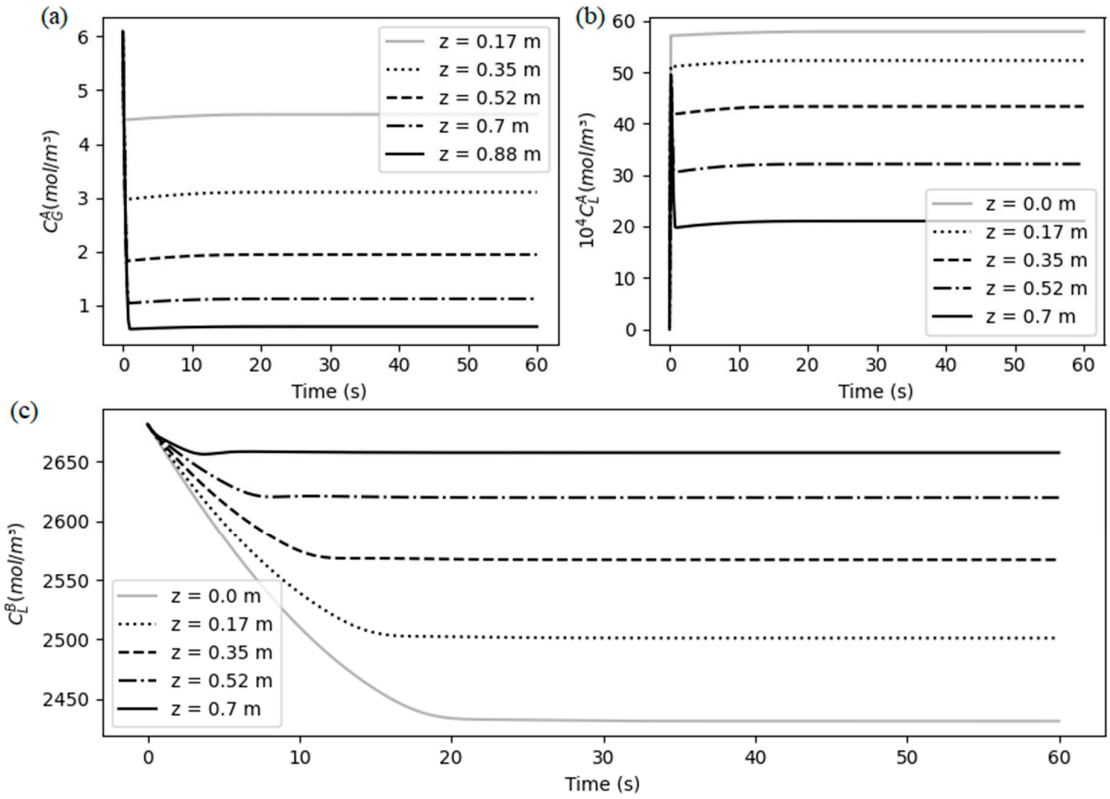

Figure 5. Solution for the CO_2 concentrations in at (a) the shell (gas phase), (b) the lumen (liquid phase) and (c) the concentration of free MEA in liquid.

An approximation of the CO_2 profiles at the first instants can be seen in Figu. 5. The concentration profiles in the gas phase, showed in Figure 6(a), follows an expected pattern, decreasing uniformly at each point of space, while the concentration in liquid, showed in Figure 6(b), suffers an immediately growth, as it was considered to be initially zero and the fast mass transfer process makes a small amount of solute appear at the liquid phase. A part of that CO_2 in liquid begins to be instantaneously consumed by the chemical reaction.

Preprints (www.preprints.org) | NOT PEER-REVIEWED | Posted: 29 December 2023 doi:10.20944/preprints202312.2309.v1

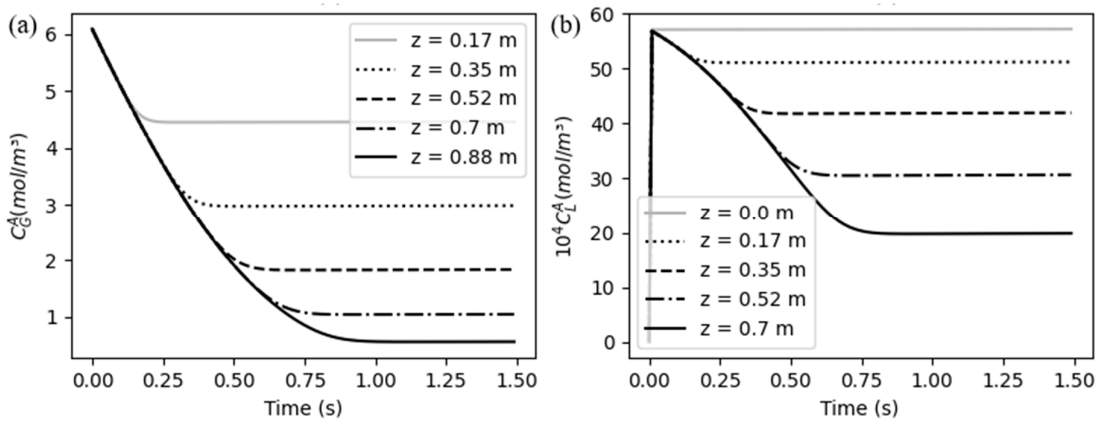

Figure 6. Initial profiles of CO_2 concentration in (a) the gas phase and (b) liquid phase.

Through the results it was also possible to obtain the CO_2 capture ratio and rich loading, as shown in Figure 7 (a) and (b), respectively. It can be seen that the capture ratio has a pattern very similar to the concentration in the gas phase (on inverted way), rinsing fast and suffering a smooth decrease after a peak, until get stable. It happens because the concentration gradient is greater at the initial instants, making the CO_2 flux reach a maximum point and decrease due the performance of the chemical reaction. On the other hand, the CO_2 rich loading performs in a smoothly pattern, just like the free MEA concentration behavior, but also on a mirror trend.

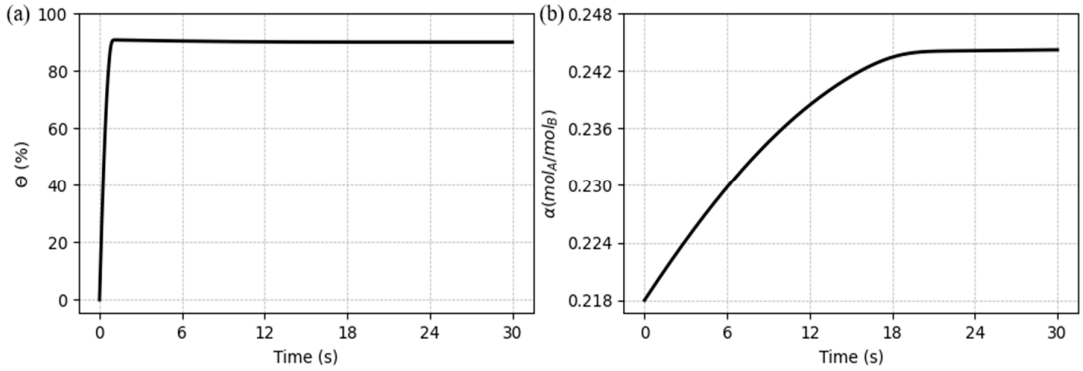

Figure 7. Initial profiles of CO_2 concentration in (a) the gas phase and (b) liquid phase.

5.2. Steady-state results

The steady-state profiles area necessary to understand to where the process goes and what is happening along the fibers. Therefore, the profiles along the fibers are shown in Figure 8 for CO_2 concentration in the gas (a) and liquid (b) phase, and the concentration of free MEA in the liquid (c). The profile for the gas is expected to decrease from its inlet side ($z = 0$), as the CO_2 migrates from the gas to the liquid. As the solvent stream enters the system without free CO_2, the solute concentration increases quickly, and grows along the z (from $z = 0.88$), although the free MEA concentration begins to decrease from $z = 0.88$, due the chemical reaction.

Preprints (www.preprints.org) | NOT PEER-REVIEWED | Posted: 29 December 2023 doi:10.20944/preprints202312.2309.v1

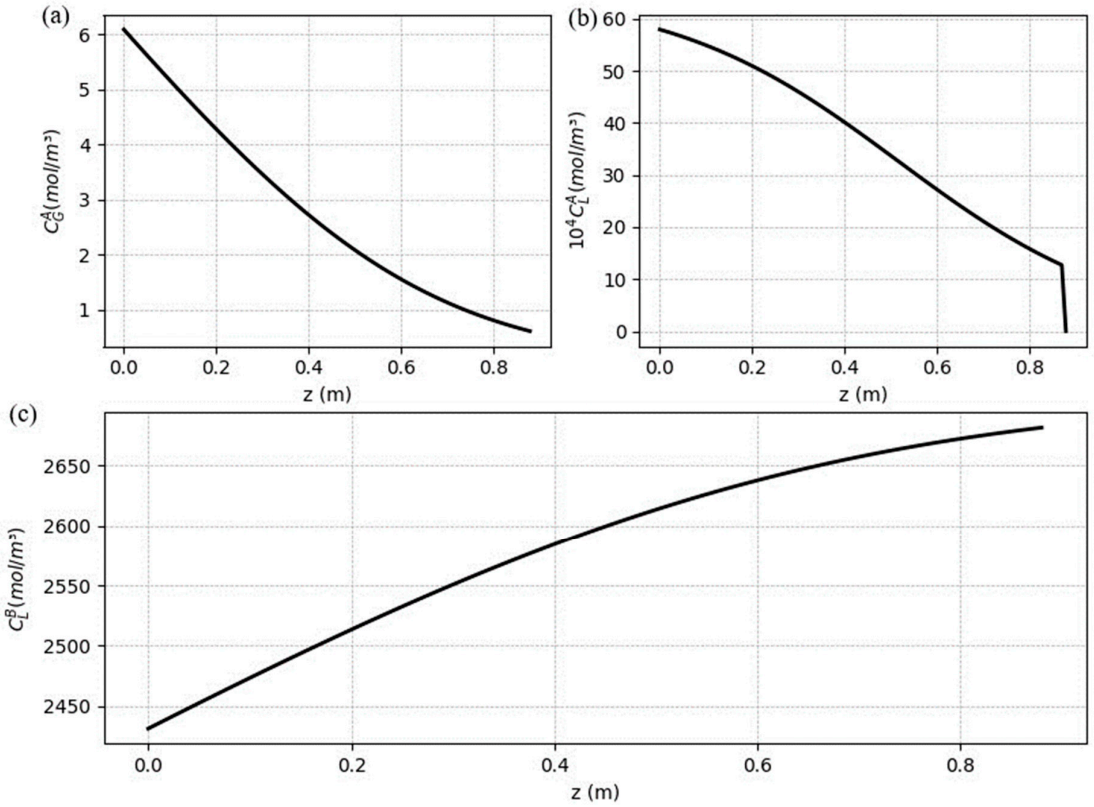

Figure 8. Steady-state profiles for CO_2 concentrations in at (a) the shell (gas phase), (b) the lumen (liquid phase) and (c) the concentration of free MEA in liquid.

The fast reaction regime can be confirmed by the profile of the ratio between the Hatta number (Ha) and the asymptotic enhancement factor (E_∞) along the membrane's length (steady state regime), as shown in Figure 9. Because the values are between 0.2 and 5, we can conclude, according to Table 3, that the reaction is characterized as fast and second order, where both the mass transfer and the

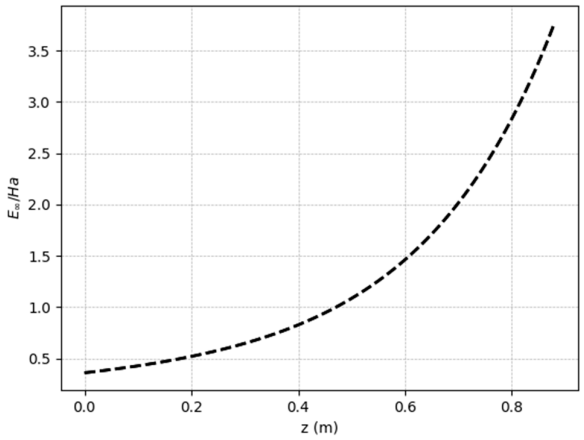

Figure 9. Reaction regime profile.

In order to verify the effectiveness of the dynamic model, a step response and pulse response experiments were designed, considering the steady state values reached in the previous section as the base case. The chosen input variables are distributed in four distinct cases: disturbances in the liquid flow rate (case 1); disturbances in the gas flow rate (case 2); disturbances in the inlet CO_2 composition (case 3); disturbances in the CO_2 lean loading (case 4).

Preprints (www.preprints.org) | NOT PEER-REVIEWED | Posted: 29 December 2023 doi:10.20944/preprints202312.2309.v1

5.3. Dynamic response to process disturbances

In order to verify the effectiveness of the dynamic model, a step response and pulse response experiments were designed, considering the steady state values reached in the previous section as the base case. The chosen input variables are distributed in four distinct cases: disturbances in the liquid flow rate (case 1); disturbances in the gas flow rate (case 2); disturbances in the inlet CO_2 composition (case 3); disturbances in the CO_2 lean loading (case 4).

5.3.1. Case 1: Disturbances in the liquid flow rate

In the Case 1, a disturbance of a ± 30% step liquid flow rate, referred to the value in Table 7, weas performed and the dynamic responses analyzed. The dynamic test results for these changes are shown in Figure 10(b) and (c).

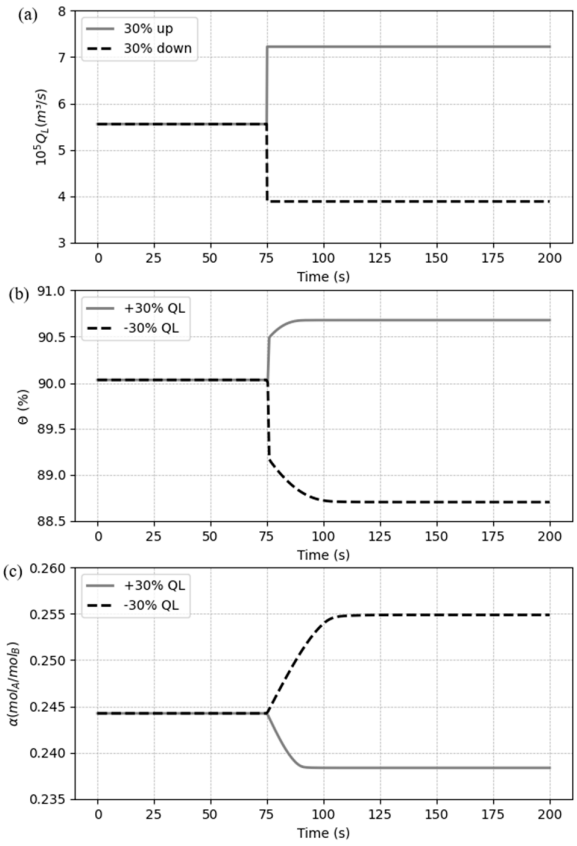

Figure 10. Step changes on liquid inlet volumetric flow rate (**a**) and responses in (**b**) CO_2 capture ratio and (**c**) CO_2 loading.

From Figure 9, we can see that, when the liquid flow rate (Q_L) increases +30%, the CO_2 capture ratio also grows instantaneously before a smooth curve, while the CO_2 loading decreases until get stable. The increment in Θ is due to solvent (MEA) addition and consequently more CO_2 uptake available and a larger amount of MEA in the solvent makes the rich loading get smaller. When the liquid flow rate is reduced by 30 percent, a similar trend is observed in opposite direction, but in a higher proportion compared to the first change. It can be concluded that the decrease in solvent flow affects the system more significantly than the increase, from the same condition.

To verify how Q_L would present a transient change in the amplitude of a signal from a baseline value to a higher or lower value, followed by a rapid return to the baseline value, a pulse signal was implemented. The pulse signal has been set with a period of 75 seconds and an amplitude of 20% of the initial value. The pulse and responses they are shown in Figure 11.

Preprints (www.preprints.org) | NOT PEER-REVIEWED | Posted: 29 December 2023 doi:10.20944/preprints202312.2309.v1

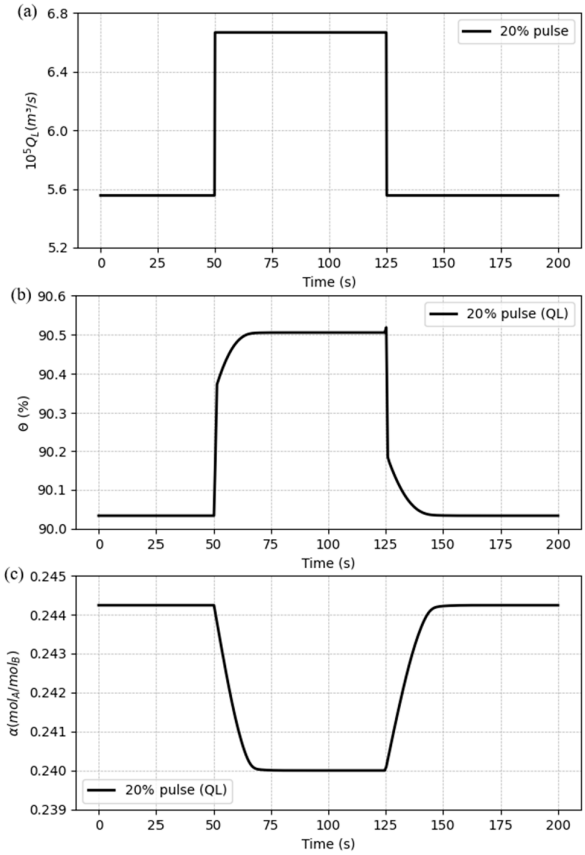

Figure 11. Pulse disturbance in liquid inlet volumetric flow rate (a) and responses in (b) CO_2 capture ratio and (c) CO_2 loading.

According to Figure 11, the model shows stable as the variables reach a stationary point and come back to the previous steady-state after the pulse. The behavior of the curves follows the expected pattern seen in the step changes for both variables.

5.3.2. Case 2: Disturbances in the gas flow rate

Similarly, to the previous case, a step response (± 30%) for the flue gas flow rate is designed and the dynamic behavior of the system is analyzed. The dynamic performances responses for Case 2 are shown in Figure 12.

Preprints (www.preprints.org) | NOT PEER-REVIEWED | Posted: 29 December 2023 doi:10.20944/preprints202312.2309.v1

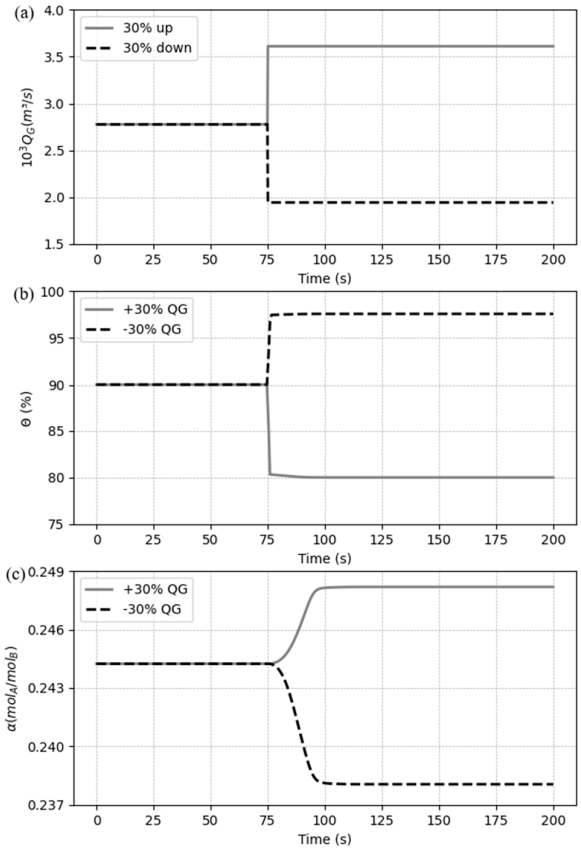

Figure 12. Step changes in inlet gas volumetric flow rate (a) and responses for (b) CO_2 capture ratio and (c) CO_2 loading.

As shown in Figure 12, CO_2 capture ratio has a quicker response compared to the CO_2 loading, and after a sharp curve, it reaches the steady state. Nevertheless, the loading only starts to change significantly right after that sharp change in capture ratio and follows smoothly to the stationary point. As the step change is applied to the gas stream and the CO_2 capture ratio is computed concentration in the gas phase, it is expected that this variable suffers the variation firstly, but only gets stable when the liquid phase reaches the permanent state. Figure 12(b) shows that, when increasing the gas flow rate, the capture ratio suffers a negative variation, and I can be explained because of the amount of gas, and consequently the amount of CO_2, rises in the system, which one has the same quantity of solvent to treat the new gas stream, reducing the capacity of the system to capture the solute. The reverse occurs when the rate is decreased, and the capture ration grows. For the CO_2, it rises as soon as more CO_2 enters the system and decrease when the gas is reduced. This behavior occurs because, although the capacity of the system to capture the same proportion of CO_2 as before is affected, the increment in the gas rate allows a greater amount of solute migrating to the liquid, and a decrement do the reverse trend. It also can be observed that, different from the case 1, the variation in the gas flow rate affects the variables in distinct proportions: when increasing, the capture ration is more affected than the loading, and the reverse happens when the input is decreased.

Also, a pulse signal was set for this case, considering an amplitude of 40% and a period time of 75 seconds, starting at the instant of 50 seconds. The pulse profile and the responses on the process variables are shown in Figure 13(a), (b) and (c).

Preprints (www.preprints.org) | NOT PEER-REVIEWED | Posted: 29 December 2023 doi:10.20944/preprints202312.2309.v1

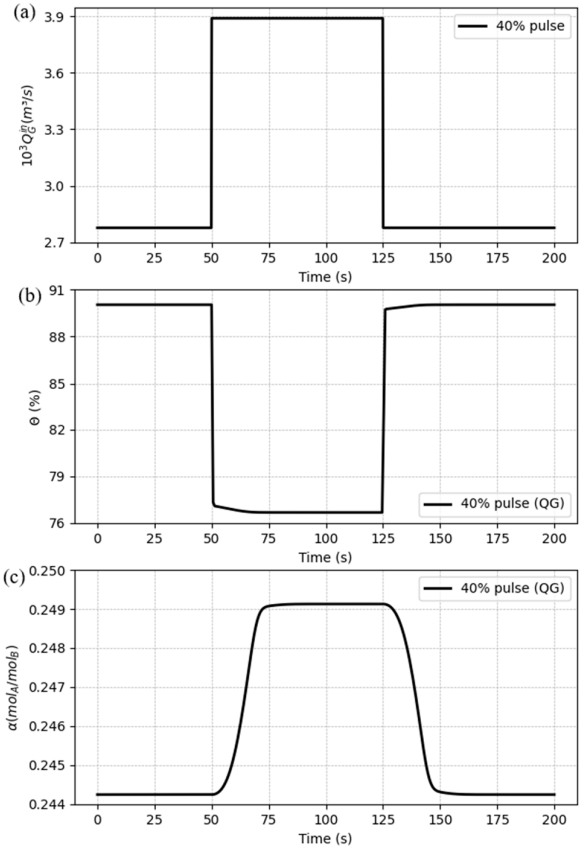

Figure 13. Pulse disturbance in gas inlet volumetric flow rate (a) and responses in (b) CO_2 capture ratio and (c) CO_2 loading.

The results patterns follow the behavior from the step changes, where the capture ratio has a sharper change (Figure 13(b)), if compared to the loading (Figure 13 (c)), who has a smooth change against the disturbances, despite that the first one takes a greater time to get stabilized. The model showed to be stable against the variation of the gas flow rate.

5.3.3. Case 3: Disturbances in the inlet CO_2 composition

The third case simulates a disturbance on the molar composition of CO2 on the flue gas (y_A^{in}). A step change of +20% of the initial value is compared with a -20% step change, as shown in Figure 14(a). The dynamic responses for Θ and α_{rich} can be observed in Figure 14(b) and (c), respectively.

The CO_2 loading response has a well-defined response to both changes, getting stable after a smooth change, increasing with the more amount of solute in the system and decreasing with the less (Figure 14(c)). On the other hand, disturbing y_A^{in} makes the CO_2 capture ratio suffers an immediately change (Eq. 12), and then keeps variating with the outlet composition of the solute (y_A^{out}). This behavior is confirmed in Figure 14(b) for both disturbances (± 20%), where Θ also presents an inverse response characteristic, initially responding in the opposite direction from the final response. Figure 15 shows what happens at the instant of the disturbance occurs.

Preprints (www.preprints.org) | NOT PEER-REVIEWED | Posted: 29 December 2023 doi:10.20944/preprints202312.2309.v1

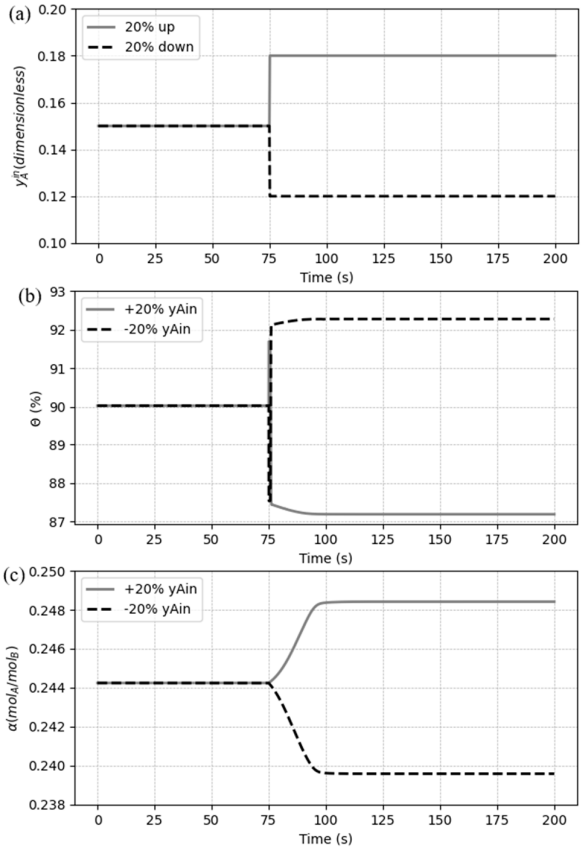

Figure 14. Step changes in inlet molar fraction of CO_2 on gas (**a**) and responses for (**b**) CO_2 capture ratio and (**c**) CO_2 loading.

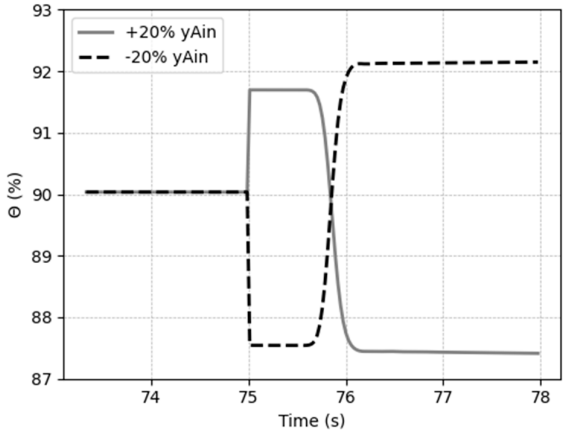

Figure 15. Zoomed response of CO_2 capture ratio against the step changes in CO_2 molar fraction.

The generated overshoot can be visualized in Figure 15, and an explanation for this behavior is the fact that changes in the composition of gas affects the concentration gradient, making a fast change in the molar flux of solute in the same direction of the step change; however, the solvent quantity to arrest the amount CO_2 does not change, leading the system to a new and opposite steady state. After reach the real direction, the capture ration keeps varying in a smoothly way until the liquid phase get stable.

A pulse disturbance was also designed for the CO_2 inlet composition in the gas, having an amplitude of 40% from the previous value and a period of 75 seconds, as shown in Figure 16(a). The CO_2 capture ratio behavior against the pulse disturbance follows a similar trend from the step

Preprints (www.preprints.org) | NOT PEER-REVIEWED | Posted: 29 December 2023 doi:10.20944/preprints202312.2309.v1

changes, including the inverse response, which has a bigger overshoot when the input variable decreases to the previous value, compared to the beginning of the pulse signal. It can be seen in Figure 16(b) that after the pulse period, it stabilizes at the same value form the beginning. Figure 16(c) shows that α also reaches back to the initial state after the pulse, showing the expected pattern.

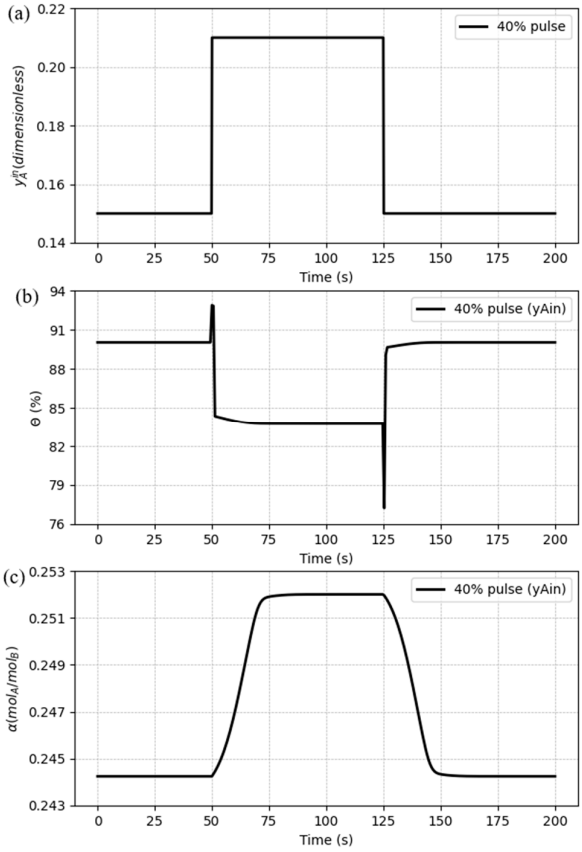

Figure 16. Pulse disturbance in the inlet gas CO_2 composition (**a**) and responses in (**b**) CO_2 capture ratio and (**c**) CO_2 loading.

5.3.3. Case 4: Disturbances in the CO_2 lean loading

The last case makes a variation in CO_2 loading at the inlet side of the HFMC. As in the previous cases, a set of step changes was defined with a ± 30% variation in relation to the base case. Figure 17 demonstrates the disturbance and shows the dynamic responses of the CO_2 capture ratio and CO_2 rich loading.

Preprints (www.preprints.org) | NOT PEER-REVIEWED | Posted: 29 December 2023 doi:10.20944/preprints202312.2309.v1

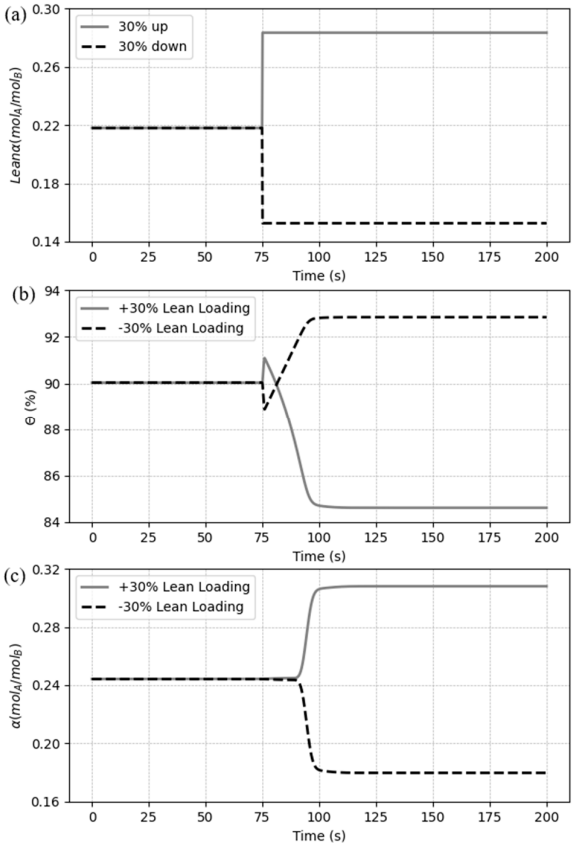

Figure 17. Step changes in lean loading of CO_2 on liquid (**a**) and responses for (**b**) CO_2 capture ratio and (**c**) CO_2 lean loading.

An inverse response in the capture ratio can also be seen by varying the lean loading of CO_2 in Figure 17(b). A change in the inlet loading of CO_2 in the liquid means a change in the concentration of free MEA in the solution. As the free MEA concentration is reduced, by increasing the lean loading of CO_2, the system is less influenced by the chemical reaction at first, which makes de outlet concentration of CO_2 in the gas also be reduced by the physical absorption, letting the capture ratio rise for a moment. However, the system's capacity to uptake the solute is reduced by the drop in the amount of MEA, so Θ decreases to a lower value compared to the base case (the opposite occurs by reducing the input variable). Figure 17(c) shows a delay in the response of the rich loading, which one follows the same direction of the variation signal. The initial variation in α_{rich} is minimal because the concentration of CO_2 along the gas phase be still processing the disturbance. Nonetheless, as soon as the gas phase follows to the proper direction, the loading begins quickly chasing the new values. As the amount of CO_2 in the solvent is changed when varying the lean loading, the quantity of solute at the outlet side is also modified, getting greater when increasing the input variable and being reduced when decreasing the same input. Yet, it can be inferred from the results that the decrease of the lean loading affects the process in a greater proportion, if compared to the increase change.

Also, a pulse variation was settled to analyze if the system can be changed and still turn back to the initial state. The disturbance designed has a period of 75 seconds and a magnitude of 40% of the initial value. The results can be seen in Figure 18.

Preprints (www.preprints.org) | NOT PEER-REVIEWED | Posted: 29 December 2023 doi:10.20944/preprints202312.2309.v1

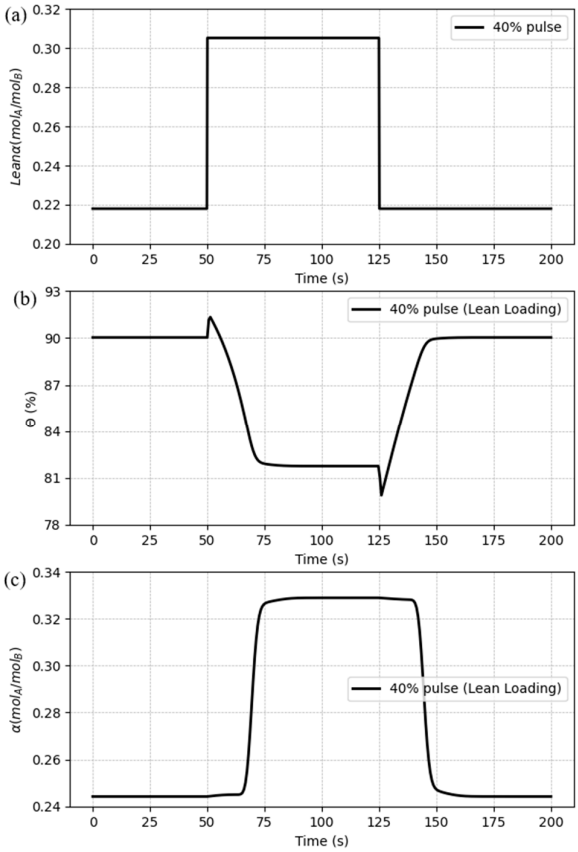

Figure 18. Pulse disturbance in the lean loading of CO_2 (**a**) and responses in (**b**) CO_2 capture ratio and (**c**) CO_2 rich loading.

For the pulse variation, the model shows to be stable, assuming the values from the base case after the disturbance ends, despite the overshoots presented by the CO_2 capture ratio and the delay in the response of the CO_2 rich loading.

5. Conclusions

This section is not mandatory but may be added if there are patents resulting from the work reported in this manuscript. This manuscript reported on a one-dimensional dynamic modeling and simulation study of CO_2 removal from a flue gas employing chemical absorption carried out in a hollow fiber membrane contactor (HFMC). For this purpose, with important model assumptions, the dynamic model responses proved to be coherently with the expected physic behavior, matching very well with the experimental data used in the validation stage.

With the results of the dynamic simulations, it was possible to evaluate the effect of some disturbances on important process variables, such as the CO_2 capture rate and CO_2 rich loading, in order to analyze the stability and capacity of the model to predict the plant behavior. The responses obtained from the step changes and pulse disturbances showed to be very distinct from one input variable to another. Regarding the settling time of responses, the gas phase showed to be faster than the liquid phase. Although, from the analyzed results, each response can be explained according to the given input variations. It was observed that the model reaches states that are coherent with the theoretically expected for all step changes and stay stable against the various pulse variations proposed. Also, as discussed, the way and proportion in which each change affects the system resulted in important information for applying future control strategies to this process.

The development of more efficient capture processes can lead to a substantial reduction in CO_2 emissions. Thus, this dynamic study motivates HFMC to reach technology readiness level on an industrial scale. Even though the literature lacks available experimental dynamic data to validate the

transient behavior of the process, once the system dynamics got satisfactory results for a wide range of operation fluctuations, different control strategies can be considered, such as advanced model predictive control (MPC). Additionally, State Observers (OS), for example, Un-scented Kalman Filter (UKF), can be applied when the model gets identified by available dynamic data from a HFMC unit for carbon capture.

Author Contributions: Conceptualization, W.P. and A.J.; methodology, W.P., A.J and L.R.; software, W.P.; validation, W.P. and J.F.; writing—original draft preparation, W.P and J.F.; writing—review and editing, W.P., A.J. and L.R.; project administration, A.J. All authors have read and agreed to the published version of the manuscript.

Funding: This research was financed by CAPES.

Institutional Review Board Statement: Not applicable.

Data Availability Statement: The data are contained within the article.

Acknowledgments: The authors are very thankful to PPGEQ, UFPB and the LABMCIP.

Conflicts of Interest: The authors declare no conflicts of interest.

References

1. Ghobadi, J.; Ramirez, D.; Khoramfar, S.; Kabir, M.M.; Jerman, R.; Saeed, M. Mathematical modeling of CO2 separation using different diameter hollow fiber membranes. *Int. J. Greenh. Gas Control* **2021,** *104*, 103204. [CrossRef].
2. Leung, D.Y.; Caramanna, G.; Maroto-Valer, M.M. An overview of current status of carbon dioxide capture and storage technologies. *Ren. Sus. Energy Reviews* **2014**, *39*, 426-443. [CrossRef]
3. Chao, C.; Deng, Y.; Dewil. R.; Baeyens, J.; Fan, X. Post-combustion carbon capture. *Renew. Sus. Energy Reviews* **2021** *138*, 110490. [CrossRef]
4. Wang, M.; Lawal, A.; Stephenson, P.; Sidders, J.; Ramshaw, C. Post-combustion CO2 capture with chemical absorption: A state-of-the-art review. *Chem. Eng. Res. Des.* **2011**, *89(9)*, 1609-1624. [CrossRef] .
5. Yan, S.P.; Fang, M.X.; Zhang, W.F.; Wang, S.Y.; Xu, Z.K.; Luo, Z.Y.; Cen, K.F. Experimental study on the separation of CO2 from flue gas using hollow fiber membrane contactors without wetting. *Fuel Process. Tech.* **2007**, *88(5)*, 501-511. [CrossRef]
6. Younas, M.; Druon-Bocquet, S.; Sanchez, J. Experimental and theoretical mass transfer transient analysis of copper extraction using hollow fiber membrane contactors. *J. Mem. Sci.* **2011**, *382(1-2)*, 70-81. [CrossRef]
7. Zhao, S.; Feron, P.H.; Deng, L.; Favre, E.; Chabanon, E.; Yan, S.; Hou, J.; Chen, V.; Qi, H. Status and progress of membrane contactors in post-combustion carbon capture: A state-of-the-art review of new developments. *J. Mem. Sci.* **2016**, 511:180-206. [CrossRef]
8. Feron, P.H.M.; Jansen, A.E. Capture of carbon dioxide using membrane gas absorption and reuse in the horticultural industry. *E. Conv. Man.* **1995**, *36(6-9)*,411-414. [CrossRef]
9. deMontigny, D.; Tontiwachwuthikul, P.; Chakma, A. Using polypropylene and polytetrafluoroethylene membranes in a membrane contactor for CO2 absorption. *J. Mem. Sci.* **2006**, *277(1-2)*, 99-107. [CrossRef]
10. Ma'mun, S.; Dindore, V.Y.; Svendsen, H.F. Kinetics of the reaction of carbon dioxide with aqueous solutions of 2-((2-aminoethyl) amino) ethanol. *Ind. Eng. Chem. Res.* **2007**, *46(2)*, 385-394. [CrossRef]
11. Atchariyawut, S.; Jiraratananon, R.; Wang, R. Mass transfer study and modeling of gas–liquid membrane contacting process by multistage cascade model for CO2 absorption. *Sep. Purif. Tech.* **2008**, *63(1)*, 15-22. [CrossRef]
12. Theo, W.L.; Lim, J.S.; Hashim, H.; Mustaffa, A.A.; Ho, W.S. Review of pre-combustion capture and ionic liquid in carbon capture and storage. *App. Energy* **2016**, *183*, 1633-1663. [CrossRef]
13. Gabelman, A.; Hwang, S.T. Hollow fiber membrane contactors. *J. Mem. Sci*. **1999**, *159(1-2)*, 61-106. [CrossRef]
14. Li, J.L.; Chen, B.H. Review of CO2 absorption using chemical solvents in hollow fiber membrane contactors. *Sep. Purif. Tech.* **2005**, *41(2)*, 109-122. [CrossRef]
15. Simons, K.; Nijmeijer, K.; Wessling, M. Gas–liquid membrane contactors for CO2 removal. *J. Mem. Sci.* **2009**, *340(1-2)*, 214-220. [CrossRef]
16. Cui, Z.; deMontigny, D. Part 7: A Review of CO2 Capture Using Hollow Fiber Membrane Contactors. *Carbon Manag*. 2013, *4*, 69–89. [CrossRef]
17. Rivero, J.R.; Panagakos, G.; Lieber, A.; Hornbostel, K. Hollow fiber membrane contactors for post-combustion carbon capture: A review of modeling approaches. *Mem.* **2020**, *10(12)*, 382. [CrossRef]
18. Mansourizadeh, A. Experimental study of CO2 absorption/stripping via PVDF hollow fiber membrane contactor. *Chem. Eng. Res. Des.* **2012**, *90(4)*, 555-562. [CrossRef]

19. Rode, S.; Nguyen, P.T.; Roizard, D.; Bounaceur, R.; Castel, C.; Favre, E. Evaluating the intensification potential of membrane contactors for gas absorption in a chemical solvent: A generic one-dimensional methodology and its application to CO2 absorption in monoethanolamine. *J. Mem. Sci.* **2012**, *389*, 1-16. [CrossRef]
20. Zaidiza, D.A.; Billaud, J.; Belaissaoui, B.; Rode, S.; Roizard, D.; Favre, E. Modeling of CO2 post-combustion capture using membrane contactors, comparison between one-and two-dimensional approaches. *J. Mem. Sci.* **2014**, *455*, 64-74. [CrossRef]
21. Khaisri, S.; deMontigny, D.; Tontiwachwuthikul, P.; Jiraratananon, R. A mathematical model for gas absorption membrane contactors that studies the effect of partially wetted membranes. *J. Mem. Sci.* **2010**, *347(1-2)*, 228-239. [CrossRef]
22. Zaidiza, D.A.; Belaissaoui, B.; Rode, S.; Neveux, T.; Makhloufi, C.; Castel, C.; Roizard, D.; Favre, E. Adiabatic modelling of CO2 capture by amine solvents using membrane contactors. *J. Mem. Sci.* **2015**, *493*, 106-119. [CrossRef]
23. Porcheron, F.; Drozdz, S. Hollow fiber membrane contactor transient experiments for the characterization of gas/liquid thermodynamics and mass transfer properties. *Chem. Eng. Sci.* **2009**, *64(2)*, 265-275. [CrossRef]
24. Pakšiová, D.; Fikar, M.; Skogestad, S. Modeling of carbon dioxide removal using membrane contactors. In 2016 Cybernetics & Informatics (K&I), Levoca, Slovakia, 2016, (pp. 1-6). [CrossRef]
25. Rosli, A.; Shoparwe, N.F.; Ahmad, A.L.; Low, S.C.; Lim, J.K. Dynamic modelling and experimental validation of CO2 removal using hydrophobic membrane contactor with different types of absorbent. *Sep. Purif. Tech.* **2019**, *219*, 230-240. [CrossRef]
26. Asadi, J.; Kazempoor, P. Dynamic response and flexibility analyses of a membrane-based CO2 separation module. International *J. Greenh. Gas Control* **2022**, *116*, 103634. [CrossRef]
27. Bozonc, A.C.; Cormos, A.M.; Dragan, S.; Dinca, C.; Cormos, C.C. Dynamic Modeling of CO2 Absorption Process Using Hollow-Fiber Membrane Contactor in MEA Solution. *Energies* **2022**, *15(19)*, 7241. [CrossRef]
28. Wattanaphan, P.; Sema, T.; Idem, R.; Liang, Z.; Tontiwachwuthikul, P. Effects of flue gas composition on carbon steel (1020) corrosion in MEA-based CO2 capture process. *Int. J. Greenh. Gas Control* **2013**, *19*, 340-349. [CrossRef]
29. D'Alessandro, D.M.; Smit, B.; Long, J.R. Carbon dioxide capture: prospects for new materials. *Angewandte Chemie International Edition* **2010**, *49(35)*, 6058-6082. [CrossRef]
30. Scholes, C.A.; Ho, M.T.; Wiley, D.E. Membrane-cryogenic post-combustion carbon capture of flue gases from NGCC. *Tech.* **2016**, *4(2)*, 14. [CrossRef]
31. Chabanon, E.; Kimball, E.; Favre, E.; Lorain, O.; Goetheer, E.; Ferre, D.; Gomez, A.; Broutin, P. Hollow fiber membrane contactors for post-combustion CO2 capture: A scale-up study from laboratory to pilot plant. *Oil & Gas Sci. Tech.–Revue d'IFP Energies nouvelles* **2014**, *69(6)*, 1035-1045. [CrossRef]
32. Kimball, E.; Al-Azki, A.; Gomez, A.; Goetheer, E.; Booth, N.; Adams, D.; Ferre, D. Hollow fiber membrane contactors for CO2 capture: modeling and up-scaling to CO2 capture for an 800 MWe coal power station. *Oil & Gas Sci. Tech.–Revue d'IFP Energies nouvelles* **2014**, 69(6):1047-1058. [CossRef]
33. Zaidiza, D.A.; Wilson, S.G.; Belaissaoui, B.; Rode, S.; Castel, C.; Roizard, D.; Favre, E. Rigorous modelling of adiabatic multicomponent CO2 post-combustion capture using hollow fiber membrane contactors. *Chem. Eng. Sci.* **2016**, *145*, 45-58. [CrossRef]
34. Zaidiza, D.A.; Belaissaoui B.; Rode, S.; Favre, E. Intensification potential of hollow fiber membrane contactors for CO2 chemical absorption and stripping using monoethanolamine solutions. *Sep. Purif. Tech.* **2017**, *188*, 38-51. [CrossRef]
35. Happel, J. Viscous flow relative to arrays of cylinders. *AIChE Journal* **1959**, *5(2)*, 174-177. [CrossRef]
36. Boucif, N.; Corriou, J.P.; Roizard, D.; Favre, E. Carbon dioxide absorption by monoethanolamine in hollow fiber membrane contactors: A parametric investigation. *AIChE journal* **2011**, *58(9)*, 2843-2855. [CrossRef]
37. Farjami, M.; Moghadassi, A.; Vatanpour, V. Modeling and simulation of CO2 removal in a polyvinylidene fluoride hollow fiber membrane contactor with computational fluid dynamics. *Chem. Eng. Processing: Process Intens.* **2015**, *98*, 41-51. [CrossRef]
38. Nakhjiri, A.T.; Heydarinasab, A.; Bakhtiari, O.; Mohammadi, T. Modeling and simulation of CO2 separation from CO2/CH4 gaseous mixture using potassium glycinate, potassium argininate and sodium hydroxide liquid absorbents in the hollow fiber membrane contactor. *J. Env. Chem. Eng.* **2018**, *6(1)*, 1500-1511. [CrossRef]
39. Wang, R.; Zhang, H.Y.; Feron, P.H.M.; Liang, D.T. Influence of membrane wetting on CO2 capture in microporous hollow fiber membrane contactors. *Sep. Purif. Tech.* **2005**, *46(1-2)*, 33-40. [CrossRef]
40. Keshavarz, P.; Fathikalajahi, J.; Ayatollahi, S. Analysis of CO2 separation and simulation of a partially wetted hollow fiber membrane contactor. *J. Haz. Mat.* **2008**, *152(3)*, 1237-1247. [CrossRef]
41. Mavroudi, M.; Kaldis, S.P.; Sakellaropoulos, G.P. A study of mass transfer resistance in membrane gas–liquid contacting processes. *J. Mem. Sci.* **2006**, *272(1-2)*, 103-115. [CrossRef]
42. Skelland, A.H.P. *Diffusional Mass Transfer*. John Wiley & Sons: New York, USA, 1974.

43. Miyatake, O.; Iwashita, H. Laminar-flow heat transfer to a fluid flowing axially between cylinders with a uniform wall heat flux. *Int. J. Heat Mass Transf.* **1991**, *34(1)*, 322-327. [CrossRef]
44. Bao, L.; Lipscomb, G.G. Mass transfer in axial flows through randomly packed fiber bundles with constant wall concentration. *J. Mem. Sci.* **2002**, *204(1-2)*, 207-220. [CrossRef]
45. Bao, L.; Lipscomb, G.G. Well-developed mass transfer in axial flows through randomly packed fiber bundles with constant wall flux. *Chem. Eng. Sci.* **2002**, *57(1)*, 125-132. [CrossRef]
46. Kreulen, H.; Smolders, C.A.; Versteeg, G. F.; Van Swaaij, W.P.M. Determination of mass transfer rates in wetted and non-wetted microporous membranes. *Chem. Eng. Sci.* **1993**, *48(11)*, 2093-2102. [CrossRef]
47. Hikita, H.; Asai, S.; Ishikawa, H.; Honda, M. The kinetics of reactions of carbon dioxide with monoethanolamine, diethanolamine and triethanolamine by a rapid mixing method. *The Chem. Eng. J.* **1977**, *13(1)*, 7-12. [CrossRef]
48. Danckwerts, P.V. The reaction of CO2 with ethanolamines. *Chem. Eng. Sci.* **1979**, 34(4):443-446. [CrossRef]
49. Beek, W.J.; Muttzall, K.M.K.; van Heuven, J.M. *Transport Phenomena*, 2nd ed. John Wiley & Sons: London, England, 1999.
50. Levenspiel, O. *Chemical Engineering Reaction*, 3rd ed. John Wiley & Sons: New York, USA, 1999.
51. Zhang, H.Y.; Wang, R.; Liang, D.T.; Tay, J.H. Modeling and experimental study of CO2 absorption in a hollow fiber membrane contactor. *J. Mem. Sci.* **2006**, *279(1-2)*, 301-310. [CrossRef]
52. Sohaib, Q.; Muhammad, A.; Younas, M.; Rezakazemi, M. Modeling pre-combustion CO2 capture with tubular membrane contactor using ionic liquids at elevated temperatures. *Sep. Purif. Tech.* **2020**, 241:116677. [CrossRef]
53. Ma'mun, S.; Svendsen, H.F. Solubility of N2O in aqueous monoethanolamine and 2-(2-Aminoethyl-amino)ethanol solutions from 298 to 343 K. *Energy Procedia* **2009**, *1(1)*, 837-843. [CrossRef]
54. Poling, B.E.; Prausnitz, J.M.; O'Connell, J.P. *The Properties of Gases and Liquids*, 5th ed. McGraw-Hill: New York, USA, 2001.
55. Weiland, R.H.; Dingman, J.C.; Cronin, D.B.; Browning, G.J. Density and viscosity of some partially carbonated aqueous alkanolamine solutions and their blends. *J. Chem. Eng. Data* **1998**, *43(3)*, 378-382. [CrossRef]
56. Maceiras, R.; Álvarez, E.; Cancela, M.A. Effect of temperature on carbon dioxide absorption in monoethanolamine solutions. *Chem. Eng. J.* **2008**, *138(1-3)*, 295-300. [CrossRef]
57. Versteeg, G.F.; Van Swaaij, W.P. Solubility and diffusivity of acid gases (carbon dioxide, nitrous oxide) in aqueous alkanolamine solutions. *J. Chem. Eng. Data* **1988**, *33(1)*, 29-34. [CrossRef]
58. Snijder, E.D.; te Riele, M.J.; Versteeg, G.F.; Van Swaaij, W.P.M. Diffusion coefficients of several aqueous alkanolamine solutions. *J. Chem. Eng. Data* **1993**, *38(3)*, 475-480. [CrossRef]
59. Versteeg, G.F.; Van Dijck, L.A.J.; van Swaaij, W.P.M. On the kinetics between CO2 and alkanolamines both in aqueous and non-aqueous solutions. An overview. *Chem. Eng. Communi.* **1996**, *144(1)*, 113-158. [CrossRef]